A Temporal-Spatial Framework for Efficient Heat Flux Monitoring of Transient Boiling

Christy Dunlap, Changgen Li, Hari Pandey, Ying Sun, and Han Hu, Member, IEEE

Abstract— Two-phase cooling offers superior heat dissipation compared to conventional single-phase cooling methods. Nevertheless, the occurrence of critical heat flux (CHF) during boiling introduces reliability concerns, potentially leading to system failure. To improve system reliability, optical imaging is employed to analyze and monitor cooling systems without disrupting the boiling dynamics. These methods involve analyzing images of the boiling process to identify boiling regimes and evaluate heat flux. However, current optical-based methods are limited to static images, thereby missing out on the valuable temporal information captured by high-speed imaging. Inspired by the successful integration of temporal information in other fields, this work aims to exploit the temporal information from transient pool boiling captured via high-speed imaging for enhanced heat flux monitoring. For this purpose, two frameworks, comprising six different machine-learning models, have been developed for a comparative analysis. Specifically, the first framework includes two models that use static images for monitoring, serving as a representation of existing methodologies and a benchmark against which the second framework is measured. The remaining four models within the dynamic imagebased framework (the 2nd framework) leverage sequences of images to capture temporal information. To evaluate the advantage of incorporating temporal information, transient boiling experiments were conducted to construct the dataset. A comparative analysis confirmed that temporal information significantly enhances the accuracy of the developed heat flux monitoring models. Among these models, the developed principal components (PCA)-convolutional neural network (CNN) stands out with a superior determination coefficient of 97.4% and a mean absolute percentage error of 7.0%, achieving an excellent balance between monitoring accuracy and computational efficiency.

Index Terms— Computer vision, condition monitoring, heat flux, image sequence, machine learning, pool boiling.

I. INTRODUCTION

HE need for high heat dissipation cooling systems is rapidly growing due to the increasing prevalence of high-power electronics, data centers [1], microelectronics [2], or electric vehicles [3]. Boiling allows for higher heat dissipation while maintaining a relatively low

This study was supported by the National Science Foundation grant number OIA-1946391 and CBET-2323022 and the University of Arkansas Chancellor's Fund for Commercialization and Chancellor's GAP Fund. This work used Bridges-2 GPU at Pittsburgh Supercomputing Center through allocation MCH200010 from the Advanced Cyberinfrastructure Coordination Ecosystem: Services & Support (ACCESS) program, which is supported by National Science Foundation grants #2138259, #2138286, #2138307, #2137603, and #2138296. C. Dunlap. appreciates the support from the Arkansas Space Grant Consortium Student Intensive Training program. (Corresponding author: Han Hu).

superheat in the nucleate boiling regime when compared to other air or liquid single-phase cooling systems. However, the usage of such boiling-based cooling systems (two-phase cooling systems) is limited by instabilities, such as the critical heat flux (CHF). When the heat flux reaches the CHF, a vapor layer covers a large portion of the heat exchange surface and acts as an insulator resulting in a rapid decline in heat transfer efficiency [4]. Consequently, the temperature can increase hundreds of degrees in a matter of seconds which can lead to overheating or burnout [5]. Therefore, it is crucial to maintain proper monitoring of the system.

Currently, there are serval ways to address the CHF situation: 1) developing micro-scale modifications to the heating surface's structure; 2) predict the CHF; and 3) maintaining proper monitoring of boiling systems. The first method aims to increase CHF to enhance safety margins and power limits. Haas et al. [6] investigated the influence of serval surface modification processes on CHF for Zircaloy-4 tubes. They find that, as the pressure and mass flow rate increase, the CHF can be up to 29% higher with surface-structured tubes featuring microchannels, porous layers, and oxide layers compared to smooth tubes. Lee and Mudawar [7] conducted subcooled flow boiling experiments in a microchannel heat sink using Hydrofluoroether 7100 as the working fluid. They find that CHF was triggered by the formation of a vapor blanket along the micro-channel walls. In this work, a system technology was developed to modify existing CHF correlations to more accurately account for the unique characteristics of microchannel heat sinks. The second method aims to provide a prediction value CHF in advance so as to avoid safety risks. Mudawar et al. [8] developed artificial neural network (ANNs) for CHF prediction in flow boiling, utilizing data from both microgravity conditions aboard the international space station and earth gravity. They analyzed a comprehensive dataset from the flow boiling and condensation experiment and demonstrated that the ANNs outperformed existing correlations highlighting its potential to enhance predictive capabilities in flow boiling applications under varied gravitational conditions. The third method aims to monitor heat flux so as to give

Ying Sun is with the Department of Mechanical and Materials Engineering, University of Cincinnati, Cincinnati, OH 45221 USA.

Christy Dunlap, Changgen Li, Hari Pandey, and Han Hu are with the Department of Mechanical Engineering, University of Arkansas, Fayetteville, AR 72701 USA. (e-mail: hanhu@uark.edu).

advanced warning and avoid thermal runaways. Dunlap et al. [9] proposed a machine learning framework for monitoring heat flux of pool boiling using acoustic signals. It was found that the fast Fourier transform-Gaussian process regression model is the most promising, exhibiting high accuracy and the lowest computational cost.

Additional complexities arise when trying to monitor boiling heat transfer. Escalating or oscillating heat loads induce transient boiling and are prevalent in several important applications. In the case of reactivity-initiated accidents, the heat load in nuclear reactors rise exponentially to trigger CHF during transient boiling [10], [11]. The high-frequency switching of microelectronic and power modules contributes to oscillating heat loads in power grids and electric vehicles [12], [13] resulting in device failure. Transient boiling is also prevalent in space applications, for example the use of cryogenics for thermal management or propulsion [14]. Motivated by the need for improving safety margins and optimizing heat transfer for these applications, further research is needed. Steady state data alone is insufficient for fully understanding transient boiling (e.g., different heat transfer mechanisms, notably higher CHF values) [15]. Therefore, transient boiling experiments and analysis are crucial. Two categories of transient boiling (i.e., fast and slow) exist. There are marked differences between the two, such as boiling regimes or CHF triggering mechanisms [16], [17]. Fast transient boiling occurs over milliseconds such that bubbles nucleating on the heating surface may not be able to depart as typical in the nucleate boiling regime. Instead, the bubbles merge and directly form a vapor layer [18]. Slow transient boiling involves gradual changes in heat load and is commonly seen in normal operation of the aforementioned applications. Although both types are relevant and important to study, slow transient boiling is studied in this work. Several complexities arise when trying to study transient boiling, including managing high temperatures and implementing high-frequency sensors (e.g., thermocouples, high speed cameras) for fast and accurate measurements.

Traditional thermal monitoring uses thermocouples to measure temperature gradients and calculate heat flux using Fourier's law [19], [20], [21], [22]. This method is limited by thermal diffusion. Also, the use of intrusive sensors (i.e., thermocouples) can interfere with boiling and make replacements difficult. Transverse thermoelectric heat flux sensors provide non-intrusive measurement [23], [24] However, they have limited frequency response and are sensitive to electromagnetic interference, which limits its applications in power electronics. Transient boiling also adds to the challenge of monitoring boiling heat flux. Therefore, there is an urgent demand for a high-frequency, non-intrusive, and non-electrical method to measure transient boiling heat flux in high-power-density electronic systems.

High-speed optical imaging has been explored in boiling characterization [25]. In this field, traditional image analysis and, more recently, computer vision techniques have been used for both qualitative and quantitative boiling analysis. Conventional image processing techniques have been used to

determine bubble properties (i.e., bubble diameter, count, departure, nucleation density, etc.) [26] and estimate void fraction [27]. Machine learning-aided computer vision techniques have been implemented with boiling image data to characterize bubble dynamics [28], [29], identify boiling regimes [30], [31] and flow regimes [32], detect dry spots [33], predict heat transfer coefficients [34] and heat flux [35]. Hobold et al. [35] used image data from a nucleate boiling experiment to train a multi-layer perceptron (MLP) and a convolutional neural network (CNN) for heat flux prediction. The multi-layer perceptron uses images transformed through principal component analysis as model input and the convolutional model directly takes raw images as input. Their test results suggest that the principal components and convolutional layers can encode boiling heat transfer mechanism information that exists within the boiling images. Scariot et al. [36] used steadystate boiling images to train a traditional CNN for boiling heat flux measurement. Experimental results demonstrate that CNN exhibits lower prediction errors under high heat flux conditions. They attribute this phenomenon to the higher frequency of bubble departure at a high heat flux state. Suh et al. [37] proposed a CNN and Mask R-CNN [38] hybrid method to extract deep features and physical features (like bubble size and count) simultaneously. Then, the fused features are used for heat flux prediction. Experiments proved that their method overtook some existing methods like MLP and CNN. Heo [39] used image sequences recorded at several different heat fluxes as input to train a classification model, and it is tested at heat fluxes seen outside the training set. Each set of training images acquired under a specific heat flux serves as a class. The final prediction is the weighted average of the heat flux of each class, with the weights derived from the output of the network's softmax layer. It's worth noting that this approach relies on steady-state boiling data, rendering it unsuitable for continuous heat flux monitoring. However, these majority of the abovementioned models only rely on static images and consequently do not account for the temporal information present within the continuous boiling images.

To sum up, optical high-speed imaging is a promising technique for high-frequency, non-intrusive cooling system monitoring. However, current methods have the following shortcomings.

- 1) They primarily focus on static frames, neglecting the dynamic information captured by high-speed photography.
- 2) The training and testing of many of these models relied solely on images obtained from steady-state boiling conditions, which means they are not suitable for transient boiling and CHF warning.
- 3) Most of the existing methods are constructed as classification models that require images obtained at extremely small heat flux intervals as input to achieve high prediction accuracy. Consequently, monitoring transient boiling heat flux effectively becomes challenging for these models.

Different from the neglect of temporal information in thermal monitoring research, many other fields have achieved success by incorporating temporal data from image sequences and integrating spatial-temporal information for predictions. Temporal-based machine learning models are used in applications such as the medical field [40], [41], environmental data prediction [42], dendrite growth in electrochemical systems [43], or defect detection [44], [45], [46]. Kim et al. [47] used different sets of features including temporal and spatial data for urban growth modeling and found that their random forest model with spatiotemporal and accessibility covariates achieved the highest accuracy. Rahman et al. [41] used the convolutional long short-term memory architecture to predict biological age from physical activity data. Knaak et al. [48] combined spatial and temporal information to classify defects on welds by using sequences of images in a convolutional neural network-gated recurrent unit model. By using the spatialtemporal information, their developed model achieves an F1 score of 95.1. Therefore, inspired by the fields mentioned above, we present a framework equipped with the capability to extract temporal-spatial information and perform heat flux regression. The contribution of this paper can be summarized as follows.

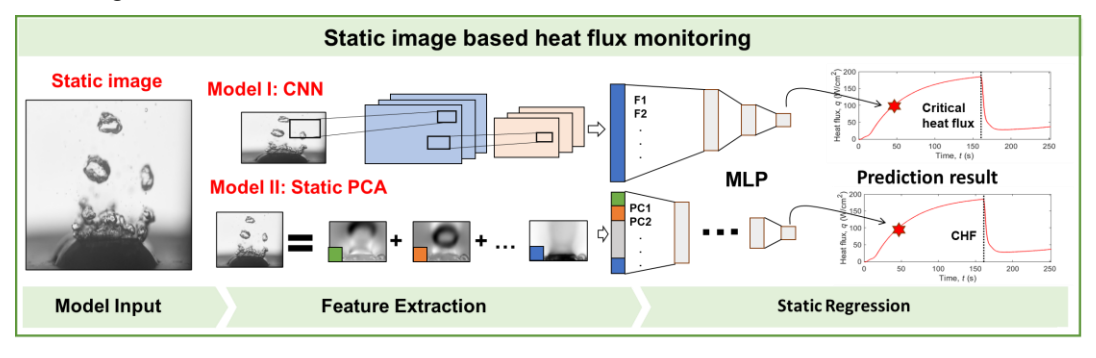
 A temporal-spatial framework is proposed. In this framework, high-speed imaging data from transient pool boiling are used as inputs and regression architectures are employed in the construction of machine learning models. The developed regression models are adopted to account for the continuously changing heat flux present in transient boiling.

- 2) A detailed comparison between the two types of pool boiling image mining framework (i.e., static image regression and sequential image regression) is presented to elucidate the impact of temporal information captured in high-speed imaging. Specifically, six different types of transient boiling heat flux regression models are generated. Among them, two models utilize only static images as input, while the others utilize image sequences. The static image-based models are used as baselines to investigate how the temporal data contained in image sequences affects model performance.
- 3) In-depth analysis is done on the top-performing model to determine the effect of dataset generation parameters (i.e., sampling rate and sequence length). Additionally, the computational time required for heat predictions is analyzed to assess the feasibility of visualization-based real-time heat flux monitoring and to demonstrate the trade-off achieved by the proposed models in terms of accuracy and efficiency.

The rest of the paper is structured as follows. Section II provides a detailed explanation of the proposed framework and boiling experiment. Section III delves into the test results and presents the comparison discussion. Lastly, Section IV offers conclusions and outlines the plan for future research.

II. METHODOLOGY

Multiple regression models were trained and tested for



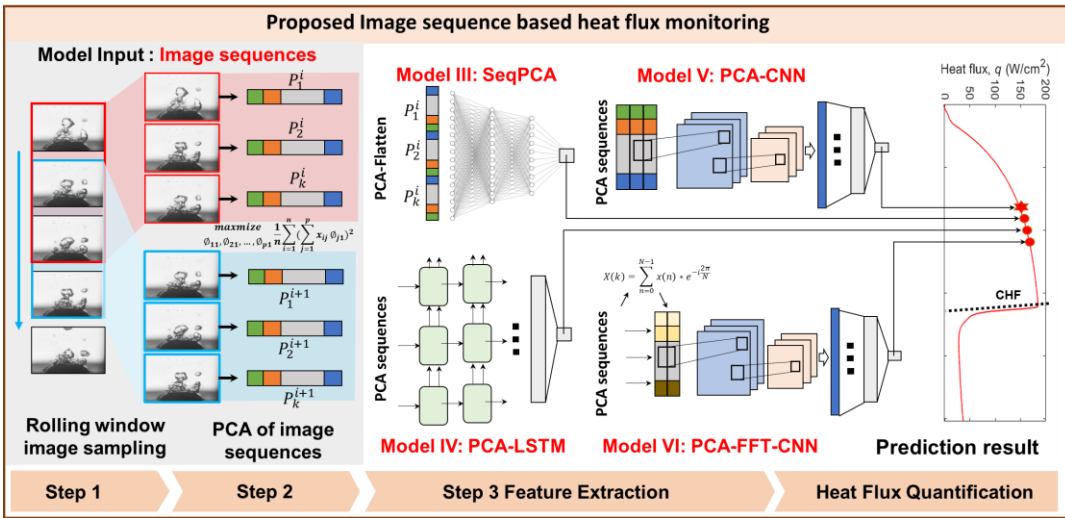


Fig.1. The developed data processing and heat flux regression models. Top panel is the static models for comparison study and the bottom panel is the proposed temporal-spatial framework based sequential models for heat flux regression.

predicting heat flux from image data. This section describes the experimental setup for collecting data, the processes used to generate multiple datasets for the models, and the model architecture for both frameworks (i.e., static and sequential). **Fig.1** shows the differences between the model types including datasets and feature extraction methods. All the regression models were written in Python using open-source libraries, Scikit-Learn [49] and TensorFlow [50].

TABLE 1
EXPERIMENTS USED FOR TRAINING, TESTING, AND VALIDATION OF MODELS.

Experiment	Usage	CHF	Vapor Escape?	Time from 0-CHF
E1	Training	136.186	Yes	175.66
E2	Training	137.34	Yes	51.43
E3	Training	112.20	No	94.48
E4	Training	107.41	No	84.33
E5	Training	100.89	No	74.53
E6	Training	97.77	No	73.48
E7	Training	109.38	No	85.03
E8	Training	106.49	No	81.88
E9	Training	104.71	Yes	77.68
E10	Validation	113.07	Yes	92.38
E11	Testing	98.12	No	70.68

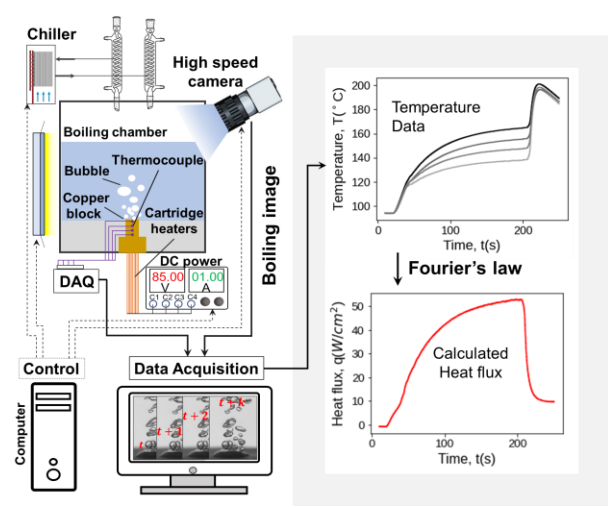


Fig.2. Transient boiling experimental setup and heat flux calculation.

A. Data Collection and Manipulation

Nucleate regime data collected from 11 separate slow transient pool boiling experiments (detailed in **Table 1**) were used for the training and testing of machine learning models. For the machine learning models, nine of the experiments were used for training, one was used for validation, and one was used for testing. The experimental set up is shown in **Fig.2** A single experiment consisted of using immersion heaters to first heat a pool of deionized water to its saturation point. Then heating a 1cm-by-1cm polished copper block submerged in the pool. The copper block was heated with nine cartridge heaters (Omega Engineering HDC19102) which were connected to a DC power supply (Magna-Power SL200-7.5). A voltage and current corresponding to a power well above the theoretical critical heat flux were applied to the cartridge heaters. For example, in an experiment with plain copper surface with theoretical CHF of

110 W/cm² (based on Zuber's limit) a power of 150 W might be applied. This is to ensure the critical heat flux is reached accounting for deviations from the theoretical CHF and losses from power to applied heat flux. After reaching the CHF (as identified by temperature spikes), the cartridge heaters were manually turned off within 3 seconds. Four T-type thermocouples, with a 3125 Hz sampling, were mounted in the side of copper block at equally spaced known heights. The heat flux at the surface was calculated using Fourier's law (q = $-k\nabla T$) under a quasi-steady state assumption. Where the temperature gradient was approximated using linear regression of the four temperature profiles. Taking into account the uncertainty from the thermocouple accuracy, thermocouple location, and linear approximation, the nucleate regime heat flux is estimated to be within 10W/cm². Owing to the relatively large thermal inertia of the copper block, transient effects on the heat flux prediction are shown to be negligible in the nucleate boiling regime [51]. A Phantom VEO 710L high-speed camera was mounted on the outside of the chamber to capture boiling images at a rate of 150 frames per second (fps). A more detailed description of the experimental facility and testing procedures can be found in [52], [53].

The images and corresponding heat flux calculations were used as input and label data for the machine-learning models. The types of models can be divided into two frameworks based on how the input data is structured, static and sequential models. Static framework refers to a single input image corresponding to a single heat flux value. Sequential framework refers to a sequence of images corresponding to a single heat flux value. To prepare the data for the models, initially, all grayscale images were resized to 200 by 200. To account for the different sampling rates of the camera and thermocouples, linear interpolation was used to approximate the heat flux value corresponding to the time of each image capture. Data for both types of frameworks were processed differently. For the static framework, each image and corresponding heat flux value was used as inputs and labels. For the sequential framework, datasets of overlapping image sequences were generated using a rolling sampling method. For each sequence of images, the heat flux approximation that corresponded to the last image in the sequence was used as the output label. For the sequential datasets, the sampling rate and sequence length were also altered for the model parametric study.

B. Static Models

Two different types of static regression models are presented here. The first is a convolutional neural network (CNN). This model used the raw boiling image as input for predicting the heat flux. The hyperband tuner from the keras tuner library was used for choosing the optimal set of hyperparameters to achieve the best validation loss. This library allows for the user to define the range of model and algorithm hyperparameters to test over. Several different models with different combinations of parameters are tested and the optimal parameters are chosen. The parameter sweep technique is introduced here to choose the filters, kernels, strides, and learning rate. The range of the sweep, step for iterating over

range, and best parameters for the CNN model are given in appendix **Table A1.1** and **A1.2**. The best parameters are the ones used in the actual model.

The next model paired principal component analysis (PCA) for feature extraction with an MLP for regression. The model is referred to as StaticPCA. PCA is an unsupervised method commonly used for data reduction. Essentially, it works by defining a new basis of eigenvectors for the images. Each image is then described as the coefficients of a linear combination of a specified amount of the new basis vectors. These coefficients are referred to as principal components (PCs). Fig.3a shows the first 25 eigenvectors for a single boiling image. These image generated using and eigenvectors were sklearn.decomposistion.PCA class fit with the training images. Fig.3b shows two original boiling images (left) and the corresponding reconstructed images using the 25 eigenvectors (right). Fig.3c shows the cumulative explained variance vs the number of PCs where

explained variance =
$$1 - \frac{variance(true-pred)}{variance(true)}$$
 (1)

Additional analysis of the performance of the staticPCA model with different quantities of PCs was also performed in the results section. The number of PCs used ranged from 1 to 900. The keras tuner was used for a parameter sweep to choose the number of neurons for the model using 900 PCs as input. This model architecture and range of parameter sweep is shown in **Table A2.1** and **A2.2**.

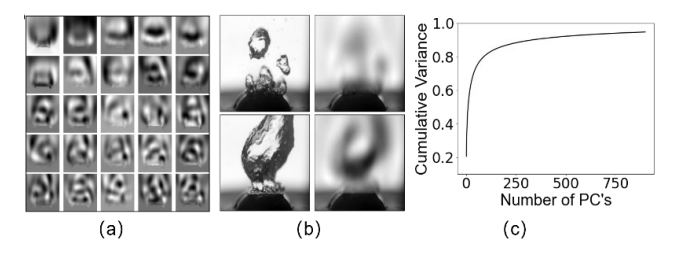


Fig.3. PCA of boiling images. (a) First 25 PCs; (b) Two representative images and reconstructed image; (c) cumulative variance vs number of pcs.

C. Sequential Models

Four types of sequential models were trained and tested. For all the sequential models, each image in a sequence (as described in the data collection and manipulations section) was first converted to a select number of PCs. Initially, all the models were trained with a sequential dataset with 40 PCs, an image sequence length of 200, and an image sampling rate of 150 fps. The first model was a multilayer perceptron. To use this model each sequence of PCs was flattened into a single dimensional array for input. This model is referred to as SeqPCA. The hyperparameter sweep range and best model are shown in Table A3.1 and A3.2. The next model used was a long short-term memory (LSTM) model. For this model, each sequence of PCs was used as input. The hyperparameter sweep range and best model are shown in Tables A4.1 and A4.2. The third model uses a CNN for regression and is referred to as PCA-CNN. First, each sequence of PCs was converted into a three-dimensional vector of shape (number of PCs, sequence

length, 1). This vector was then used as input to the convolutional layers. The parameter sweep was used to determine what kernels, filters, and strides were best. The hyperparameter sweep range and best model are shown in **Table A5.1** and **A5.2**. Due to the high performance of this model, more analysis was done on it with differing dataset parameters (i.e., sampling rate, number of PCs, and sequence length). The last model was similar to the previous one, with the only difference being that each sequence of PCs was converted to frequency intensities using the fast Fourier transform. This cut down the size of the input to the convolutional layers to (number of PCs, sequence length/2, 1). This model is referred to as PCA-FFT-CNN and the hyperparameter sweep range and best model is given in **Table A6.1** and **A6.2**.

III. RESULTS AND DISCUSSION

A. Model performance

After training and testing the six different models, their performance was compared using the test data. Two different metrics were used to compare the models, determinate coefficient (R²) and mean absolute percentage error (MAPE). Here, they are defined as

$$R^{2} = 1 - \frac{\sum_{i=1}^{n} (true_{i} - pred_{i})^{2}}{\sum_{i=1}^{n} (true_{i} - mean)^{2}}$$
 (2)

$$MAPE = \frac{1}{n} \sum_{i=1}^{n} \frac{|true_i - pred_i|}{|true_i|}$$
 (3)

Both of these metrics describe how well the models are able to predict the heat flux. The R² score is a measurement of how closely the model fits the data. Ideally, the R² score would be close to one indicating the model fits the data well. The MAPE is a measure of how much a prediction would on average vary from the true value. A lower percentage error is desired and indicates the prediction is close to the true value on average.

Fig.4a shows the R² score for all six models (static and sequential models) on the testing data. With respect to the R² score, all the sequential models performed better than the static models. Of the static models, the highest-performing model was the Static PCA with an R² score of 0.858. However, the higher R² score of the SeqPCA, 0.916, implies that the temporal information carried by the image sequences improves the heat flux mapping capabilities. From these values, it can further be seen that the PCA-CNN model had the best performance with a R² score of 0.974. Fig.4b shows the MAPE for all of the models. The models with the lowest MAPE are the SeqPCA, PCA-LSTM, PCA-FFT-CNN, and PCA-CNN with values of 10%, 7.8%, 9.7%, and 7% respectively. When comparing StaticPCA to SeqPCA, a significant decrease in MAPE is observed, further demonstrating that the model based on image sequences outperforms the one based on static images in terms of predictive accuracy.

The static image method directly extracts features from each frame. Compared to StaticPCA, CNN, as a representative network, has a similar R² and lower MAPE. This result indicates that CNN has better nonlinear feature extraction capability than StaticPCA. However, when comparing the static

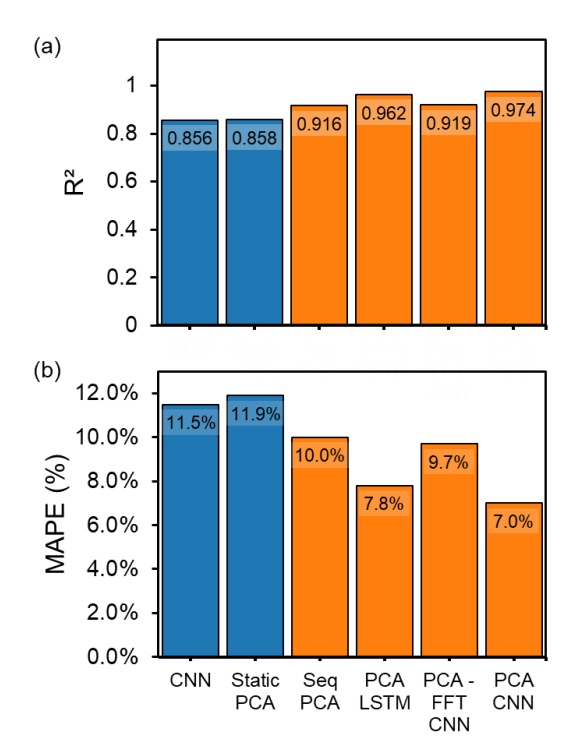


Fig.4. R² and MAPE for all six regression models using the test data.

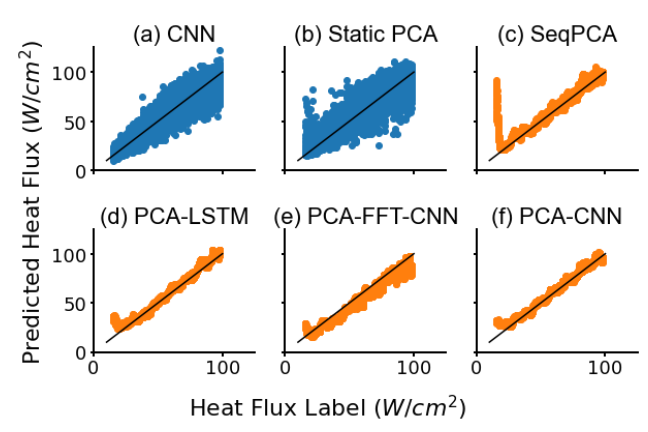


Fig.5. Plots of predicted heat flux vs true heat flux label for two static regression (a, b) and four sequential regression (c-f) models.

CNN with the image sequence-based PCA-CNN, it can be seen that the latter outperforms the former in both metrics. This is because PCA-CNN retains the powerful nonlinear feature extraction capability of CNN while having better temporal information extraction ability. Additionally, the introduction of PCA reduces the noise interference in the input data. Comparing PCA-FFT-CNN with PCA-CNN, it can be found that the introduction of frequency domain information even deteriorates the accuracy of heat flux regression. These frequency domain features increase the difficulty for CNN in extracting deep abstract features. LSTM is mainly used for processing sequential data and is good at capturing temporal dependencies and long-term relationships. However, LSTM is not as efficient as CNN in extracting spatial features from images. Therefore, the R² and MAPE metrics of PCA-LSTM are inferior to those of PCA-CNN.

Fig.5 shows plots of predicted vs true heat flux values for all the models. Ideally, each point would lie on the diagonal black line indicating that each prediction is the same as the true heat flux. These plots are shown to verify the quantitative comparisons shown in Fig.4. From these plots, it can be seen that the PCA-CNN model appears to follow the diagonal line the closest with less variation as the previously discussed R² score and MAPE comparison would suggest. Compared to models that use only static images, the image sequences-based models exhibit smaller prediction variances, indicating they possess greater stability in monitoring heat flux.

More interestingly, it can be observed from Fig.5 (b to f) that at lower heat flux levels, the predictions of these models show an obvious deviation from the actual values especially for SeqPCA. As the heat flux increases, the precision of prediction improves. This phenomenon is consistent with the research conducted by Scariot et al.,[36] which suggests that bubble activity diminishes at lower heat flux levels. The essence of heat flux monitoring via optical imaging lies in uncovering the relationship between bubble dynamics and heat flux. Therefore, diminished bubble activity at lower heat fluxes contributes to decreased accuracy in optical imaging-based monitoring. However, as the heat flux escalates, bubble activity intensifies, thereby swiftly improving the model's precision. On the other hand, PCA is a linear dimensionality reduction method which capture features that have a linear relationship with the input while reducing signal noise. However, it may lose some nonlinear features that are crucial during low heat flux phases. These lost features can be particularly important during low heat flux phases, leading to larger prediction errors. From the comparison of (a) and (b), it can be seen that when using CNN on static images, the predictions did not show significant deviations under low heat flux conditions, whereas using PCA did. This phenomenon indicates that at lower heat flux, boiling is dominated by numerous isolated bubbles. At this stage, there is a higher-order nonlinear relationship between the bubbles and heat flux. In small-area pool boiling conditions, as the heat flux increases to a certain point, the isolated bubbles merge into mushroom-shaped formations. During this mushroom-shape phase, bubble changes are more stable, and the nonlinear relationship with heat flux is of a lower order than during the isolated bubble boiling phase, resulting in smaller regression errors. This viewpoint is further supported by the comparison of (c) and (d, e, f). Fig. 5 (c) shows the prediction results using only PCA for dimensionality reduction followed by a shallow MLP for regression, whereas figures (d, e, f) use deeper networks and more advanced nonlinear feature extraction methods after PCA. These networks better mitigate the errors caused by linear extraction in PCA during low heat flux phases. Additionally, it can be found that when using SeqPCA, the prediction results under low heat flux showed better monotonicity compared to Static PCA. This also demonstrates that the proposed spatiotemporal framework can better capture the temporal relationships between boiling images at adjacent heat flux.

Furthermore, the StaticPCA model for this initial comparison used 900 PCs so to check how added PCs will

affect the performance, the StaticPCA model was trained with different amounts of PCs. **Fig.6** shows how the R² and MAPE vary with different numbers of PCs (up to 900 PCs) for the StaticPCA models. It is seen that as the number of PCs increases, the R² score generally increases and the MAPE generally decreases until they begin to level off.

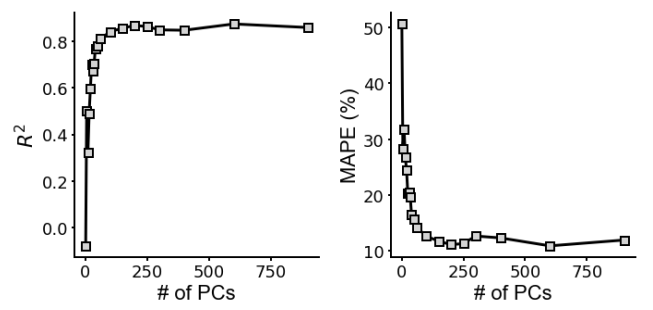
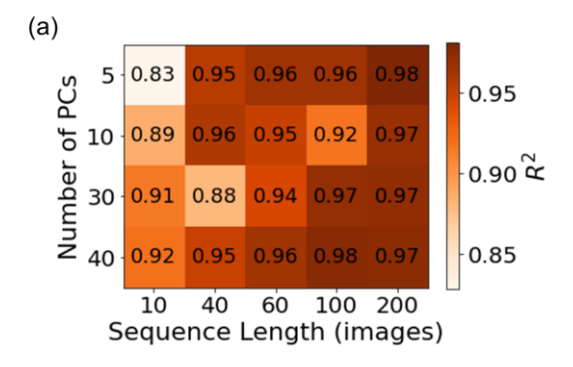


Fig.6. R² and MAPE vs # of PCs for the StaticPCA model.



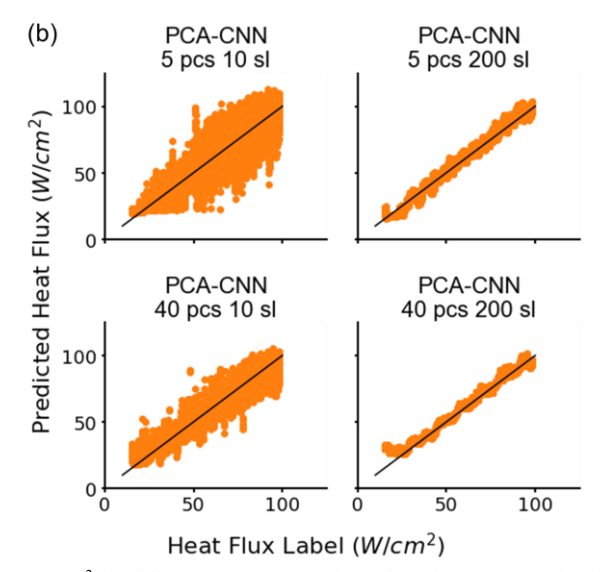


Fig.7. (a) R² for different sequence lengths and number of PC's using the PCA-CNN model architecture (b) representative plots of predicted heat flux vs heat flux label.

One primary goal of this work was to determine the differences in the model accuracy when using solely spatial information and when incorporating temporal data. **Fig.7** shows how the R² value changes with different amounts of spatial and temporal information. The PCA-CNN model was used for this test. **Fig.7a** shows how the R² varies as the amount of spatial (number of PCs) and temporal information (sequence length)

changes. From this plot, it is seen that in general as the sequence length increases, the R² score increases too. On the other hand, when the sequence length at 10, the prediction performance increase with increase of the number of PCs. However, when the sequence length higher than 40, the increase of the number of PCs do not affect the prediction performance. This phenomenon indicates both the spatial and temporal information influence the prediction, but their importance is different at different given conditions. Fig.7b shows plots of true labels vs predicted labels for the models corresponding with the four corners of the plot in Fig.7a. When comparing these predictions vs true plots, it is seen that from left to right the prediction points decrease in sparsity or, in other words, the predictions more closely reside on the diagonal line such that the heat flux predictions are closer to the labels. Similar to the spatial data, the R² score increases as more temporal data is added. It is also seen that the R2 score for the temporal data surpasses that of the spatial data. Based on the above discussion, it can be concluded that incorporating temporal information significantly enhances the model's stability and accuracy in predicting heat flux. This improvement can be attributed to the capture of dynamic bubble features, an inference also validated by the research from Won's lab [54].

B. Parametric Study of PCA-CNN Model

Among the tested machine learning models, the PCA-CNN model was found to feature a high R² score and a relatively low MAPE and is thus selected as the base model to investigate the role of sequence length and sampling rate. The goal of this parametric study is to see which sequence length and sampling rate yield the most optimal performance of the model. To understand how the sequence length and consequently how the temporal length impacts the results, downsampled datasets corresponding to sampling rates of 150, 75, 50 30, 25, and 15 fps were used to train the PCA-CNN model with different sequence lengths. Fig.8 shows the test results. Fig.8a shows the R² score vs sequence length for different sampling rates. It can be seen that as the sequence length increases in general so does the R² for all sampling rates. **Fig.8b** shows the same data as 8a but is converted to the temporal length instead. The smaller sampling rates cover more time with fewer images than larger sampling rates. The temporal length is calculated by

$$t_{seq} = \frac{Sequence\ Length}{Sampling\ Rate} \tag{4}$$

By doing this, it is observed that all the sampling rates except 15 fps collapse into a single line. This implies that, down to a certain sampling rate, if a sequence of images covers the same amount of time, they will have similar performance. This trend, however, is not carried out forever; at a specific sampling rate, the rate will be too low and as a result, the image sequences will lose important information used in the predictions. **Fig.8c** shows the MAPE vs sequence length for the different artificial sampling rates. It can be seen that in general, the MAPE decreases as the sequence length increases. **Fig.8d** shows the same data as **Fig.8c** but converted to temporal length. Similar to the R² score data, the results for 25 fps and higher sampling rates begin to collapse to around the same value while the

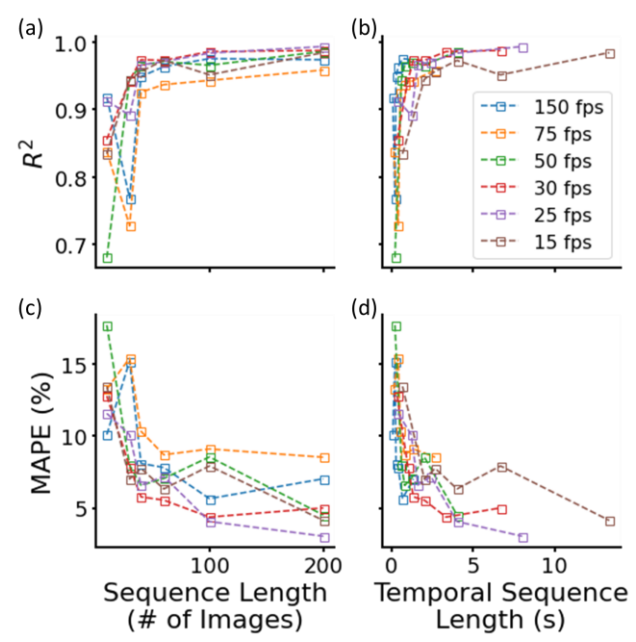


Fig.8. R² and MAPE vs sequence length and temporal sequence length for different image sampling rates.

results for the 15-fps data lie above the rest. This result reveals that if the sequence of images with a sampling rate of at least 25 fps covers almost 3.4 s of time, the model will yield very high heat flux prediction accuracy. Beyond this length of sequence sample, the performance becomes saturated and additional time information will not significantly improve the model prediction accuracy. Additionally, short sequence lengths are shown to have poor performance, which further shows the importance of additional temporal information. These results also indicate that image sequences captured at 15 fps may not cover sufficient detailed information on bubble dynamics for accurate heat flux predictions. As such, there may exist a critical sampling rate between 15 fps and 25 fps. Therefore, if the same accuracy can be made with lower sampling rates or fewer images it can lead to processing speed improvement and camera cost reduction. It should be noted that these experiments are based on slow transient boiling experiments, so these findings are not expected to hold for faster ramp up times.

C. Prediction Time of Static Image and Sequence Models

Fig.9 shows the prediction time of boiling heat flux using trained static image models (time per image) and image sequence models (time per image sequence) base models. All the models were tested on the same computer with a 12th Gen Intel Core i9-12900k processor and 2 GeForce RTX 3090 GPUs. The prediction times include preprocessing time for PCA transformation and FFT when used. One thing to note is that the time for the sequential models only includes the processing time for one image PCA transformation. Due to the overlapping image sequences, as each sequence is made using a stride of 1 then only the newest image would need to be converted to PCs and the previous transformed images can be used for the complete sequence. The CNN and PCA-LSTM models require the longest prediction times. The fastest models for prediction

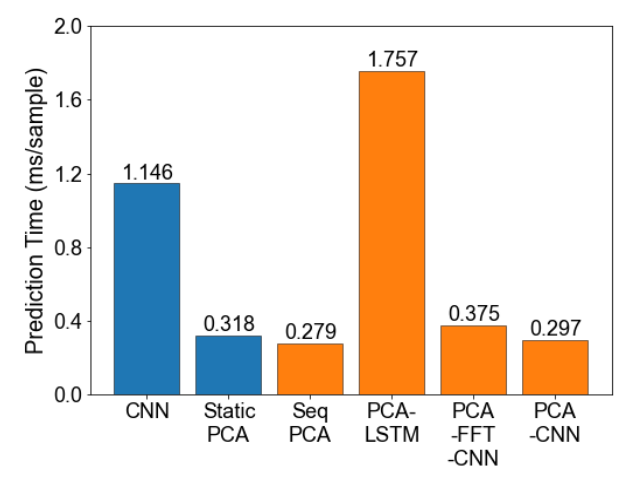


Fig.9. Prediction time for the six regression models.

time were the SeqPCA and PCA-CNN models. Comparisons indicate that utilizing PCA for image preprocessing enhances the efficiency of feature extraction while maintaining the accuracy and stability of predictions, making it suitable for heat flux monitoring that relies on high-speed imaging.

IV. CONCLUSION

In this work, two machine learning frameworks are developed for heat flux predictions using static images and image sequences, respectively. Each framework has incorporated a variety of feature extraction and regression methods to optimize the prediction accuracy. Based on the experiment results the following conclusion can be draw:

- 1) The proposed temporal-spatial framework based sequential models have better overall performance when compared with the static models. Among the sequential models, the PCA-CNN is found to have best performance with a high R2 value of 0.974, low MAPE of 7%, and low prediction time.
- 2) As the temporal length of image sequences increases, the predictions become more accurate shown by a higher R² and lower MAPE.
- 3) The effect of the sampling rate on the heat flux prediction is unpronounced for sampling rates beyond 15 fps. This observation indicates that the dynamic features of the bubbles at this frequency band are most critical to heat transfer.

Overall, this work highlights the role of temporal information of bubble dynamics in boiling heat transfer and identifies the sampling rate range needed for accurate heat flux predictions. The analysis of the prediction time confirms the viability of real-time boiling heat flux monitoring using the proposed PCA-equipped image sequence models. It should be noted that this work is built upon the combination of a heating structure of polished plain copper and deionized water. However, initial conditions like the heating surface structure, fluid character, and heating rate may influence the transient boiling procedures. In the future work, a deeper investigation will be conducted to find out whether and how these conditions impact the heat flux prediction based on the temporal-spatial framework.

APPENDIX

TABLE A1.1

STATIC CNN MODEL ARCHITECTURE WHERE ALL HYPERPARAMETERS (HP#)

ARE FOUND IN BEST COLUMN IN TABLE A1.2.

Layer (type)	Output	Filters	Kernel	Strides	Neurons	Activation
Input	(200,200,1)	-	-	-	-	-
Conv2d	(198,198,62)	hp1	hp2	hp3	-	hp4
Max Pooling	(65,65,62)	-	hp5	hp6	-	-
Dropout (0.2)	(65,65,62)	-	-	-	-	-
Conv2D	(61,61,162)	hp7	hp8	hp9	-	hp4
Max Pooling	(20,20,162)	-	hp10	hp11	-	-
Conv2D	(6,6,282)	hp12	hp13	hp14	-	hp4
Global average	(282)	-	_	_		_
Pooling	(202)	-	-	-	-	-
Dropout (0.2)	(282)	-	-	-	-	-
Dense	(501)	-	-	-	hp15	hp16
Dense	(301)	-	-	-	hp17	hp16
Dense	(1)	-	-	-	1	-

TABLE A1.2
HYPERPARAMETER SWEEP RANGE AND SELECTED PARAMETERS FOR STATIC
CNN REGRESSION AFTER PARAMETER SWEEP.

Variable	Min	Max	Stride	Options	Best
hp1	32	400	10	-	63
hp2	3	5	2	-	3
hp3	1	3	2	-	1
hp4	-	-	-	'relu','tanh'	Relu
hp5	2	6	2	-	6
hp6	1	4	2	-	3
hp7	32	500	10	-	162
hp8	3	5	2	-	5
hp9	1	3	2	-	1
hp10	2	6	2	-	4
hp11	1	4	2	-	3
hp12	32	300	10	-	282
hp13	3	5	2	-	3
hp14	1	4	2	-	3
hp15	1	1000	100	-	501
hp16	-	-	-	'relu', 'tanh'	Relu
hp17	1	1000	100	-	301

 $\begin{tabular}{ll} Table~A2.1\\ Model~architecture~for~the~static~PCA~model~using~900~pcs~where~all~hyperparameters~(hp#)~are~found~in~best~column~in~Table~A2.2. \end{tabular}$

Layer (type)	Output Shape	Neurons	Activation
Input	(900)	-	-
Dense	(1700)	hp1	Relu
Dense	(1000)	hp2	Relu
Dense	(100)	hp3	Relu
Dense	(800)	hp4	Relu
Dense	(600)	hp5	Relu
Dense	(1)	1	-

TABLE A2.2

HYPERPARAMETER SWEEP RANGE AND SELECTED PARAMETERS FOR THE STATIC PCA MODEL USING 900 PCS.

	STITTIE I	or rivious some	0,00165	
Variable	Min	Max	Stride	Best
hp1	100	2000	100	1700
hp2	100	2000	100	1000
hp3	100	2000	100	100
hp4	100	2000	100	800
hp5	100	2000	100	600

TABLE A3.1

MODEL ARCHITECTURE FOR SEQ-PCA MODEL WITH DATASET CORRESPONDING TO 40 PCS AND 200 SEQUENCE LENGTH WHERE ALL HYPERPARAMETERS (HP#) ARE FOUND IN BEST COLUMN IN TABLE A3.2.

Layer (type)	Output Shape	Neurons	Activation
Input	(8000)	-	
Dense	(500)	hp1	Relu
Dropout (0.2)	(500)	-	-
Dense	(1300)	hp2	Relu
Dense	(50)	hp3	Relu
Dense	(1850)	hp4	Relu
Dropout (0.2)	(1850)	-	-
Dense	(1)	1	-

Table A3.2

Hyperparameter sweep range and selected parameters for Seq-PCA model with dataset corresponding to 40 PCs and 200 sequence length.

	ELIGITI.					
Variable	Min	Max	Stride	Best		
hp1	100	3000	100	500		
hp2	100	2000	100	1300		
hp3	50	2000	100	50		
hp4	50	2000	100	1850		

TABLE A4.1

MODEL ARCHITECTURE FOR PCA-LSTM MODEL WITH DATASET CORRESPONDING TO SEQUENCE LENGTHS OF 200 AND 40 PCS WHERE ALL HYPERPARAMETERS (HP#) ARE FOUND IN BEST COLUMN IN TABLE A4.2.

Layer (type)	Output Shape	Units/ Neurons	Activation
Input	(200, 40)	-	
LSTM	(200, 590)	hp1	Tanh
Dropout (0.2)	(200,590)	-	
LSTM	(200,990)	hp2	Tanh
LSTM	(200, 490)	hp3	Tanh
Dropout (0.2)	(200,490)	-	
LSTM	(200,930)	hp4	Tanh
Dropout (0.2)	(200,930)	-	
LSTM	(200,190)	hp5	Tanh
Dropout (0.2)	(200,190)	-	
LSTM	(560)	hp6	Tanh
Dense	(260)	hp7	Relu
Dense	(440)	hp8	Relu
Dense	(120)	hp9	Relu
Dense	(870)	hp10	Relu
Dense	(1)	1	

TABLE A4.2

HYPERPARAMETER SWEEP RANGE AND SELECTED PARAMETERS FOR PCA-LSTM MODEL WITH DATASET CORRESPONDING TO SEQUENCE LENGTHS OF 200 AND 40 PCS.

Variable	Min	Max	Stride	Best
hpl	10	1000	10	590
hp2	10	1000	10	990
hp3	10	1000	10	490
hp4	10	1000	10	930
hp5	10	1000	10	190
hp6	10	1000	10	560
hp7	10	1000	10	260
hp8	10	1000	10	440
hp9	10	1000	10	120
hp10	10	1000	10	870

Table A5.1

Model architecture for PCA-CNN model corresponding to dataset with 40 pcs and 200 sequence length where all hyperparameters (hp#) are found in best column in Table A5.2.

Layer (type)	Output Shape	Filters	Kernel	Strides	Padding	Neurons	Activation
Input	(200,40,1)	-	-	-	-	-	-
Conv2D	(66,13,72)	hp1	hp2	hp3	None	-	Relu
Dropout (0.2)	(66,13,72)	-	-	-	-	-	-
Conv2D	(66,13,72)	hp4	hp5	hp6	Same	-	Relu
Conv2D	(22,5,92)	hp7	hp8	hp9	Same	-	Relu
Max Pooling	(11,3,92)	-	2	1	Same	-	-
Conv2D	(11,3,62)	hp10	hp11	hp12	Same	-	Relu
Dropout (0.2)	(11,3,62)	-	-	-	-	-	-
Flatten	(2046)	-	-	-	-	-	-
Dense	(181)	-	-	-	-	hp13	Relu
Dense	(931)	-	-	-	-	hp14	Relu
Dense	(1)	-	-	-	-	1	-

TABLE A5.2

HYPERPARAMETER SWEEP RANGE AND SELECTED PARAMETERS FOR PCACNN MODEL CORRESPONDING TO DATASET WITH 40 PCS AND 200 SEQUENCE
LENGTH

		LENGIH		
Variable	Min	Max	Stride	Best
hpl	32	100	10	72
hp2	3	5	2	3
hp3	1	3	2	3
hp4	32	100	10	72
hp5	3	5	2	5
hp6	1	3	2	1
hp7	32	100	10	92
hp8	3	5	2	5
hp9	1	3	2	3
hp10	32	100	10	62
hp11	3	5	2	3
hp12	1	3	2	1
hp13	1	1000	10	181
hp14	1	1000	10	931

TABLE A6.1

MODEL ARCHITECTURE FOR PCA-FFT-CNN MODEL WITH DATASET CORRESPONDING TO 40 PCS AND 200 SEQUENCE LENGTH WHERE ALL HYPERPARAMETERS (HP#) ARE FOUND IN BEST COLUMN IN TABLE A6.2.

Layer (type)	Output Shape	Filters	Kernel	Strides	Padding	Neurons	Activation
Input	(100,40,1)	-	-	-	-	-	-
Conv2D	(34,14,72)	hpl	hp2	hp3	None	-	Relu
Dropout (0.2)	(34,14,72)	-	-	-	-	-	-
Conv2D	(34,14,62)	hp4	hp5	hp6	Same	-	Relu
Conv2D	(34,14,42)	hp7	hp8	hp9	Same	-	Relu
Max Pooling	(17,7,42)	-	2	1	Same	-	-
Conv2D	(17,7,42)	hp10	hp11	hp12	Same	-	Relu
Dropout (0.2)	(17,7,42)	-	-	-	-	-	-
Flatten	(4998)	-	-	-	-	-	-
Dense	(851)	-	-	-	-	hp13	Relu
Dense	(321)	-	-	-	-	hp14	Relu
Dense	(1)	-	-	-	-	1	-

TABLE A6.2

HYPERPARAMETER SWEEP RANGE AND SELECTED PARAMETERS FOR PCAFFT-CNN MODEL WITH DATASET CORRESPONDING TO 40 PCs and 200
SEQUENCE LENGTH.

Be	Stride	Max	Min	Variable
72	10	100	32	hp1
3	2	5	3	hp2
3	2	3	1	hp3
62	10	100	32	hp4
3	2	5	3	hp5
1	2	3	1	hp6
42	10	100	32	hp7
3	2	5	3	hp8
1	2	3	1	hp9
42	10	100	32	hp10
5	2	5	3	hp11
1	2	3	1	hp12
85	10	1000	1	hp13
32	10	1000	1	hp14

REFERENCES

- [1] Q. Zhang *et al.*, "A survey on data center cooling systems: Technology, power consumption modeling and control strategy optimization," *Journal of Systems Architecture*, vol. 119, p. 102253, 2021.
- [2] M. D. Clark, J. A. Weibel, and S. V Garimella, "Impact of pressure drop oscillations on surface temperature and critical heat flux during flow boiling in a microchannel," *IEEE Trans Compon Packaging Manuf Technol*, vol. 11, no. 10, pp. 1634–1644, 2021.
- [3] C. Roe *et al.*, "Immersion cooling for lithium-ion batteries—A review," *J Power Sources*, vol. 525, p. 231094, 2022.
- [4] R. Karwa, *Heat and mass transfer*. Springer Nature, 2020.
- [5] V. P. Carey, Liquid-vapor phase-change phenomena: an introduction to the thermophysics of vaporization and condensation processes in heat transfer equipment. CRC Press, 2020.
- [6] C. Haas, F. Kaiser, T. Schulenberg, and T. Wetzel, "Critical heat flux for flow boiling of water on microstructured Zircaloy tube surfaces," *Int J Heat Mass Transf*, vol. 120, pp. 793–806, May 2018, doi: 10.1016/J.IJHEATMASSTRANSFER.2017.12.077.
- [7] J. Lee and I. Mudawar, "Critical heat flux for subcooled flow boiling in micro-channel heat sinks," *Int J Heat Mass Transf*, vol. 52, no. 13–14, pp. 3341–3352, Jun. 2009, doi:
 - 10.1016/J.IJHEATMASSTRANSFER.2008.12.019.
- [8] I. Mudawar, S. J. Darges, and V. S. Devahdhanush, "Prediction technique for flow boiling heat transfer and critical heat flux in both microgravity and Earth gravity via artificial neural networks (ANNs)," *Int J Heat Mass Transf*, vol. 220, p. 124998, Mar. 2024, doi: 10.1016/J.IJHEATMASSTRANSFER.2023.124998.
- [9] C. Dunlap, H. Pandey, E. Weems, and H. Hu, "Nonintrusive Heat Flux Quantification Using Acoustic Emissions During Pool Boiling," *Appl Therm Eng*, p. 120558, Apr. 2023, doi: 10.1016/j.applthermaleng.2023.120558.

- [10] A. Kossolapov *et al.*, "The boiling crisis of water under exponentially escalating heat inputs in subcooled flow boiling at atmospheric pressure," *Int J Heat Mass Transf*, vol. 160, p. 120137, 2020.
- [11] N. Baudin, C. Colin, P. Ruyer, and J. Sebilleau, "Transient convective boiling: analysis of experimental results," in *NURETH-16 International Topical Meeting on Nuclear Reactor Thermal Hydraulics, Hyatt Regency Chicago*, 2015, pp. 8–30.
- [12] J. Mathew and S. Krishnan, "A review on transient thermal management of electronic devices," *J Electron Packag*, vol. 144, no. 1, p. 10801, 2022.
- [13] M. Pecht and J. Gu, "Physics-of-failure-based prognostics for electronic products," *Transactions of the Institute of Measurement and Control*, vol. 31, no. 3–4, pp. 309–322, 2009.
- [14] K. Yuan, "CRYOGENIC BOILING AND TWO-PHASE CHILLDOWN PROCESS UNDER TERRESTRIAL AND MICROGRAVITY CONDITIONS," 2006.
- [15] N. Baudin, C. Colin, P. Ruyer, and J. Sebilleau, "TRANSIENT CONVECTIVE BOILING: ANALYSIS OF EXPERIMENTAL RESULTS."
- [16] M. He, E. Villarreal, H. Ban, and M. Chen, "Boiling heat transfer experiments under power transients for LWRs: A review study," Nov. 01, 2021, *Elsevier Ltd.* doi: 10.1016/j.pnucene.2021.103952.
- [17] R. Visentini, C. Colin, and P. Ruyer, "Experimental investigations on heat transfer in transient boiling," in ASME 2012 Heat Transfer Summer Conf. Collocated with the ASME 2012 Fluids Engineering Div. Summer Meeting and the ASME 2012 10th Int. Conf. on Nanochannels, Microchannels and Minichannels, HT 2012, 2012, pp. 223–231. doi: 10.1115/HT2012-58245.
- [18] V. Bessiron, T. Sugiyama, and T. Fuketa, "Clad-to-coolant heat transfer in nsrr experiments," *J Nucl Sci Technol*, vol. 44, no. 5, pp. 723–732, 2007, doi: 10.1080/18811248.2007.9711861.
- [19] D. Mani, S. Sivan, H. M. Ali, and U. K. Ganesan, "Investigation to improve the pool boiling heat transfer characteristics using laser-textured copper-grooved surfaces," *International Journal of Photoenergy*, vol. 2020, pp. 1–8, 2020.
- [20] H. Dong et al., "All-ceramic Heat-Flux Sensor for Continuous Measurement Under High Temperature and Harsh Environmental Conditions," IEEE Trans Instrum Meas, 2023.
- [21] K. Yang, "A new calibration technique for thin-film gauges and coaxial thermocouples used to measure the transient heat flux," *IEEE Trans Instrum Meas*, vol. 71, pp. 1–9, 2021.
- [22] J. Ji, B. Yan, B. Wang, and M. Ding, "Error of thermocouple in measuring surface temperature of blade with cooling film," *IEEE Trans Instrum Meas*, vol. 71, pp. 1–12, 2022.
- [23] L. A. Konopko, A. A. Nikolaeva, T. E. Huber, and A. K. Kobylianskaya, "Miniaturized heat-flux sensor based on a glass-insulated Bi–Sn microwire," *Semiconductors*, vol. 53, pp. 662–666, 2019.

- [24] S. Levikari *et al.*, "Improving energy expenditure estimation in wrist-worn wearables by augmenting heart rate data with heat flux measurement," *IEEE Trans Instrum Meas*, vol. 70, pp. 1–8, 2021.
- [25] M. T. Hughes, G. Kini, and S. Garimella, "Status, challenges, and potential for machine learning in understanding and applying heat transfer phenomena," *J Heat Transfer*, vol. 143, no. 12, p. 120802, 2021.
- [26] J. P. McHale and S. V Garimella, "Nucleate boiling from smooth and rough surfaces—Part 2: Analysis of surface roughness effects on nucleate boiling," *Exp Therm Fluid Sci*, vol. 44, pp. 439–455, 2013.
- [27] U. Puli and A. K. Rajvanshi, "An image analysis technique for determination of void fraction in subcooled flow boiling of water in horizontal annulus at high pressures," *Int J Heat Fluid Flow*, vol. 38, pp. 180–189, 2012.
- [28] B. Zajec, L. Cizelj, and B. Končar, "Experimental Analysis of Flow Boiling in Horizontal Annulus—The Effect of Heat Flux on Bubble Size Distributions," *Energies (Basel)*, vol. 15, no. 6, p. 2187, 2022.
- [29] A. Rokoni, L. Zhang, T. Soori, H. Hu, T. Wu, and Y. Sun, "Learning new physical descriptors from reduced-order analysis of bubble dynamics in boiling heat transfer," *Int J Heat Mass Transf*, vol. 186, p. 122501, 2022.
- [30] C. Dunlap, H. Pandey, and H. Hu, "Supervised and Unsupervised Learning Models for Detection of Critical Heat Flux During Pool Boiling," in *Heat Transfer Summer Conference*, American Society of Mechanical Engineers, 2022, p. V001T08A004.
- [31] F. Al-Hindawi *et al.*, "A Generalized Framework for Critical Heat Flux Detection Using Unsupervised Image-to-Image Translation," *URL: https://arxiv.org/abs/2212.09107. doi*, vol. 10, 2022.
- [32] B. Yang *et al.*, "Computer vision and machine learning methods for heat transfer and fluid flow in complex structural microchannels: a review," *Energies (Basel)*, vol. 16, no. 3, p. 1500, 2023.
- [33] M. Ravichandran, A. Kossolapov, G. M. Aguiar, B. Phillips, and M. Bucci, "Autonomous and online detection of dry areas on a boiling surface using deep learning and infrared thermometry," *Exp Therm Fluid Sci*, vol. 145, p. 110879, 2023.
- [34] A. Pare and S. K. Ghosh, "Surface qualitative analysis and ANN modelling for pool boiling heat transfer using Al2O3-water based nanofluids," *Colloids Surf A Physicochem Eng Asp*, vol. 610, p. 125926, 2021.
- [35] G. M. Hobold and A. K. da Silva, "Visualization-based nucleate boiling heat flux quantification using machine learning," *Int J Heat Mass Transf*, vol. 134, pp. 511–520, 2019.
- [36] V. K. Scariot, G. M. Hobold, and A. K. da Silva, "Data-driven diagnostics of boiling heat transfer on flat heaters from non-intrusive visualization," *Appl Therm Eng*, p. 123068, 2024.
- [37] Y. Suh, R. Bostanabad, and Y. Won, "Deep learning predicts boiling heat transfer," *Sci Rep*, vol. 11, no. 1, p. 5622, 2021.

- [38] K. He, G. Gkioxari, P. Dollár, and R. Girshick, "Mask r-cnn," in *Proceedings of the IEEE international conference on computer vision*, 2017, pp. 2961–2969.
- [39] C. Heo, Deep Learning Strategies for Pool Boiling Heat Flux Prediction Using Image Sequences. University of Arkansas, 2021.
- [40] Y. Wang, L. Sun, and D. Peng, "A multihead convlstm for time series classification in ehealth industry 4.0," *Wirel Commun Mob Comput*, vol. 2022, 2022.
- [41] S. A. Rahman and D. A. Adjeroh, "Deep learning using convolutional LSTM estimates biological age from physical activity," *Sci Rep*, vol. 9, no. 1, p. 11425, 2019.
- [42] X. Shi, Z. Chen, H. Wang, D.-Y. Yeung, W.-K. Wong, and W. Woo, "Convolutional LSTM network: A machine learning approach for precipitation nowcasting," Adv Neural Inf Process Syst, vol. 28, 2015.
- [43] R. Kumar, T. Dhara, H. Hu, and M. Chakraborty, "Visualization-based prediction of dendritic copper growth in electrochemical cells using convolutional long short-term memory," *Energy and AI*, vol. 10, p. 100203, 2022.
- [44] C. Li, L. Guo, H. Gao, and Y. Li, "Similarity-measured isolation forest: Anomaly detection method for machine monitoring data," *IEEE Trans Instrum Meas*, vol. 70, pp. 1–12, 2021.
- [45] C. Li, L. Guo, Y. Lei, H. Gao, and E. Zio, "A signal segmentation method for CFRP/CFRP stacks drilling-countersinking monitoring," *Mech Syst Signal Process*, vol. 196, p. 110332, 2023, doi: https://doi.org/10.1016/j.ymssp.2023.110332.
- [46] C. Li, Y. Lei, L. Guo, E. Zio, H. Gao, and B. Yang, "GMM-BinSeg: A Data Segmentation Method for CFRP/Aluminum Stacks Drilling-Countersinking Monitoring Signal," *IEEE Trans Instrum Meas*, 2024.
- [47] Y. Kim, A. Safikhani, and E. Tepe, "Machine learning application to spatio-temporal modeling of urban growth," *Comput Environ Urban Syst*, vol. 94, p. 101801, 2022.
- [48] C. Knaak, J. von Eßen, M. Kröger, F. Schulze, P. Abels, and A. Gillner, "A spatio-temporal ensemble deep learning architecture for real-time defect detection during laser welding on low power embedded computing boards," *Sensors*, vol. 21, no. 12, p. 4205, 2021
- [49] F. Pedregosa *et al.*, "Scikit-learn: Machine learning in Python," *the Journal of machine Learning research*, vol. 12, pp. 2825–2830, 2011.
- [50] M. Abadi et al., "{TensorFlow}: a system for {Large-Scale} machine learning," in 12th USENIX symposium on operating systems design and implementation (OSDI 16), 2016, pp. 265–283.
- [51] R. Olabiyi, H. Pandey, H. Hu, and A. Iquebal, "A Bayesian Spatio-Temporal Modeling Approach to the Inverse Heat Conduction Problem," in *Heat Transfer Summer Conference*, American Society of Mechanical Engineers, 2023, p. V001T15A005.
- [52] H. Pandey, W. Waldo, and H. Hu, "Non-Intrusive Cooling System Fault Detection and Diagnostics Using Acoustic Emission," in *Heat Transfer Summer*

- Conference, American Society of Mechanical Engineers, 2022, p. V001T09A004.
- [53] H. Pandey, H. Mehrabi, A. Williams, C. Mira-Hernández, R. H. Coridan, and H. Hu, "Electrochemical Control of Copper Foam Synthesis for Critical Heat Flux Enhancement During Boiling," *Available at SSRN 4382894*.
- [54] S. Chang *et al.*, "BubbleMask: Autonomous visualization of digital flow bubbles for predicting critical heat flux," *Int J Heat Mass Transf*, vol. 217, p. 124656, 2023.



Christy Dunlap is a Ph.D. candidate in the Department of Mechanical Engineering at the University of Arkansas. She received her B.S. in Mechanical Engineering and B.S. in Mathematics from the University of Arkansas in 2021. Her research covers machine learning aided analysis of boiling heat transfer.



Changen Li received a B.S. degree in mechatronic engineering from Xihua University, Chengdu, China, in 2018. He is a Ph.D. at the Southwest Jiaotong University, Chengdu, China, and a joint Ph.D. at Politecnico di Milano, Italy. At present, he is a research fellow at the University of Arkansas, USA. His research interests are manufacturing

monitoring signal processing and machine vision inspection.



Hari Pandey is a Ph.D. candidate in the Department of Mechanical Engineering at the University of Arkansas. He received his B.S. in Mechanical Engineering from Tribhuvan University, Nepal in 2017. His research topics include two-phase heat transfer, thermal management, electronics cooling, and machine learning.



Ying Sun is currently Herman Schneider Professor and Head of the Department of Mechanical and Materials Engineering at the University of Cincinnati. Prior to joining UC, she was Hess Family Endowed Chair Professor in Mechanical Engineering at Drexel University. In 2019-2022, Dr. Sun served as Program Director of the Thermal Transport

Processes Program at the National Science Foundation. Dr. Sun is an ASME Fellow and a recipient of the NSF CAREER Award, AFOSR Summer Faculty Fellowship, French CNRS Visiting Professorship, and Drexel College of Engineering Research Achievement Award. She serves as an Associate Editor for Journal of Heat and Mass Transfer and Journal of Electrochemical Energy Conversion and Storage, Chair of

Mechanical Engineering Department Heads and Chairs (MEDHC) Committee, and ASME International Mechanical Engineering Congress & Exposition (IMECE) Steering Committee. Dr. Sun was an Executive Leadership in Academic Technology and Engineering (ELATE) Fellow and a visiting professor at Princeton University, Ecole Polytechnique, and Tsinghua University. Dr. Sun directs the Complex Fluids & Multiphase Transport Laboratory that focuses on advancing fundamental thermal-fluid, interfacial, and data sciences, and applying them to enable efficient energy conversion and storage systems, sustainable manufacturing, and effective thermal management solutions. She co-chairs the Gordon Conference for Micro and Nanoscale Phase Change Phenomena 2025 and leads an NSF REU Site on Decarbonization.



Han Hu (Member, IEEE) is an Assistant Professor in the Department of Mechanical Engineering at the University of Arkansas. Dr. Hu received his B.S. in Theoretical and Applied Mechanics from the University of Science and Technology of China in 2011 and his Ph.D. in Mechanical Engineering from Drexel University in 2016. He was a

postdoctoral researcher at the Cooling Technologies Research Center at Purdue University from 2016 to 2019 and joined the University of Arkansas in August 2019. His research centers on two-phase flows, electronic packaging, acoustic sensing, and machine learning.